Article

Influence of Y Doping on Catalytic Activity of CeO$_2$, MnO$_x$, and CeMnO$_x$ Catalysts for Selective Catalytic Reduction of NO by NH$_3$

Eleonora La Greca [1], Tamara S. Kharlamova [2], Maria V. Grabchenko [2], Valery A. Svetlichnyi [3], Giuseppe Pantaleo [1], Luca Consentino [1], Olga A. Stonkus [4], Olga V. Vodyankina [2,*] and Leonarda Francesca Liotta [1,*]

[1] Institute for the Study of Nanostructured Materials (ISMN), National Research Council (CNR), Via Ugo La Malfa 153, 90146 Palermo, Italy; eleonora.lagreca@ismn.cnr.it (E.L.G.)

[2] Laboratory of Catalytic Research, Tomsk State University, Lenin Ave. 36, 634050 Tomsk, Russia; kharlamova83@gmail.com (T.S.K.); marygra@mail.ru (M.V.G.)

[3] Laboratory of Advanced Materials and Technology, Tomsk State University, Lenin Ave. 36, 634050 Tomsk, Russia

[4] Boreskov Institute of Catalysis SB RAS, Lavrentiev Ave. 5, 630090 Novosibirsk, Russia

* Correspondence: vodyankina_o@mail.ru (O.V.V.); leonardafrancesca.liotta@cnr.it (L.F.L.)

Abstract: Novel yttrium-doped CeO$_2$, MnO$_x$, and CeMnO$_x$ composites are investigated as catalysts for low-temperature NH$_3$-SCR. The study involves the preparation of unmodified oxide supports using a citrate method followed by modification with Y (2 wt.%) using two approaches, including the one-pot citrate method and incipient wetness impregnation of undoped oxides. The NH$_3$-SCR reaction is studied in a fixed-bed quartz reactor to test the ability of the prepared catalysts in NO reduction. The gas reaction mixture consists of 800 ppm NO, 800 ppm NH$_3$, 10 vol.% O$_2$, and He as a balance gas at a WHSV of 25,000 mL g^{-1} h^{-1}. The results indicate that undoped CeMnO$_x$ mixed oxide exhibits significantly higher deNO$_x$ performance compared with undoped and Y-doped MnO$_x$ and CeO$_2$ catalysts. Indeed, yttrium presence in CeMnO$_x$ promotes the competitive NH$_3$-SCO reaction, reducing the amount of NH$_3$ available for NO reduction and lowering the catalyst activity. Furthermore, the physical-chemical properties of the prepared catalysts are studied using nitrogen adsorption/desorption, XRD, Raman spectroscopy, temperature-programmed reduction with hydrogen, and temperature-programmed desorption of ammonia. This study presents a promising approach to enhancing the performance of NH$_3$-SCR catalysts at low temperatures that can have significant implications for reducing NO emissions.

Keywords: NO; selective catalytic reduction; manganese oxide; cerium oxide; yttrium

1. Introduction

Nitrogen oxides (NO$_x$), which include NO$_2$ and NO, are highly detrimental to human health and the environment. These emissions, commonly released by road vehicles, maritime transport, and industrial activities, contribute to a range of problems such as acid rain, photochemical smog, and ozone depletion [1–3]. Additionally, they can cause respiratory diseases in humans. To address these issues, governments have implemented stringent regulatory acts aimed at reducing atmospheric emissions [1–3]. In pursuit of this goal, numerous technologies, including electron beam processes [4], low-temperature adsorption [5], wet oxidative scrubbing (WOS) [6], NO$_x$ storage-reduction (NSR) [1], and selective catalytic reduction (SCR) [1,7], are under investigation. Innovative approaches such as electron beam processes, low-temperature adsorption, and WOS offer promising solutions to efficiently reduce and eliminate harmful nitrogen oxide pollutants from industrial emissions. However, these emerging technologies still face some limitations, such as

energy consumption and wastewater treatment costs. To further enhance their applicability, ongoing investigation and research are required. Conversely, SCR technology has emerged as one of the most advanced, economical, and effective options to reduce NO_x emissions from diesel engines, both from mobile and stationary sources. The system that operates in the presence of excess oxygen employs a reducing agent, typically ammonia (NH_3-SCR) or urea solution (urea-SCR), which undergoes hydrolysis to produce ammonia in situ [7]. In the presence of catalysts, this reaction enables the NO_x conversion to nitrogen (N_2) and water (H_2O) through the following overall reaction:

$$4NH_3 + 4NO + O_2 \rightarrow 4N_2 + 6H_2O.$$
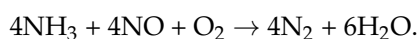
Among the catalysts that are currently under investigation, the V_2O_5-WO_3/TiO_2 composite is the most widely used in the SCR reaction. This is due to its high activity at medium temperatures (in the range of 300–400 °C), excellent chemical stability of the titania support, and good resistance to SO_2 poisoning [8]. Despite its widespread use, this catalyst possesses some intrinsic drawbacks that require further searching for alternative systems. These limitations include a narrow operating temperature range [9,10], low selectivity towards N_2 at higher temperatures, high toxicity of V_2O_5, which sublimes above 500 °C, leading to health concerns [11], and the transformation of TiO_2 support from anatase to rutile at high temperatures [12]. Thus, there is a strong need to develop new, non-vanadium-based catalysts that demonstrate high performance, good hydrothermal stability, and are not susceptible to poisoning by exhaust components.

Oxide-based materials, particularly mixed oxides, have recently attracted significant interest as potential catalysts for the reduction of NO_x emissions from diesel engine exhaust gases [9,13]. Manganese oxide (MnO_x), in particular, has been extensively investigated due to its ability to convert NO_x at low temperatures, variable valence states, and excellent oxygen migration ability that facilitates NO oxidation to NO_2. However, the practical application of manganese-based catalysts is limited by their low N_2 selectivity, poor resistance to H_2O and sulfur, and narrow operating temperature window, which requires further improvements [14,15].

Cerium oxide (CeO_2), a material that has been successfully employed in various reactions, has also shown promise in eliminating NO_x emissions due to its good redox properties and high oxygen storage/release capacity resulting from oxygen vacancies in the material and the Ce^{4+}/Ce^{3+} redox couple. In addition, CeO_2 has a low cost and low environmental impact. The NO_x adsorption by catalysts, the NO oxidation to NO_2, the strength of Brønsted acid sites, and the water and sulfur resistances can all be enhanced by using CeO_2, all of which are crucial and beneficial for the NH_3-SCR reaction [16,17].

Several studies [18–23] have reported that the combination of cerium and manganese oxides can improve the catalytic activity and sulfur tolerance in the NH_3-SCR reaction of NO_x. This improvement is attributed to the promotion of redox reactions between Ce and Mn species as well as the improvement of oxygen mobility and storage capacity [24].

In addition to the combination of Ce and Mn oxides, the use of dopants to further enhance the catalytic activity and stability of various materials has been suggested. Dopants with ionic radius and electronegativity similar to those of supports have been identified as suitable candidates to modify the physical-chemical properties. Several studies have reported that the redox capacity, oxygen vacancy and mobility, surface area, hydrothermal stability, and SO_2 tolerance of various oxides can be significantly improved due to doping with rare-earth metals [25–27]. In the case of ceria, doping with trivalent rare-earth ions such as Y^{3+} results in the incorporation and enrichment of these ions within the CeO_2 lattice. Y^{3+} is highly stable, and its valence state is lower than that of Ce^{4+}. Thus, the CeO_2 doping with Y can increase the concentration of oxygen vacancies to compensate for the negative charge, leading to the formation of a defective structure that improves the mobility of the oxygen lattice [25].

Based on the above studies, the aim of this work is to explore the potential to use manganese oxide (MnO_x), cerium oxide (CeO_2), and mixed oxide ($CeMnO_x$) that have been

previously studied as supports for Ag catalysts in the selective catalytic reduction of NO with hydrocarbons (HC-SCR) [28] in the NO-SCR by NH_3, as well as to estimate the impact of yttrium doping on the materials' performance.

2. Results and Discussion

Table 1 lists the samples studied. The citrate sol-gel method was used to synthesize the undoped oxides (samples designated as CeO_2, MnO_x, and $CeMnO_x$), while two synthesis methods were employed to prepare the Y-doped materials, i.e., an impregnation of the prepared undoped oxides with an aqueous solution of $Y(NO_3)_3$ (samples designated as Y/CeO_2, Y/MnO_x, $Y/CeMnO_x$) and a one-pot sol-gel citrate method (samples designated as $Y-CeO_2$, $Y-MnO_x$, $Y-CeMnO_x$). The catalysts were characterized by a complex of methods such as low-temperature nitrogen adsorption, X-ray diffraction (XRD), Raman spectroscopy, temperature-programmed reduction with H_2 (H_2-TPR), and temperature-programmed desorption of ammonia (NH_3-TPD), to evaluate and compare physical properties and chemistries of the materials. The real composition of the samples was similar to the nominal one.

Table 1. Chemical composition, specific surface area (SSA), and total pore volume (V) of materials studied.

Sample	Content (wt.%)			Ce/Mn	SSA (m^2/g)	V (cm^3/g)
	Y	Ce	Mn			
CeO_2	-	80.6	-	-	40	0.14
Y/CeO_2	2.7	78.6	-	-	32	0.13
$Y-CeO_2$	1.8	79.5	-	-	43	0.16
MnO_x	-	-	72.7	-	14	0.12
Y/MnO_x	3.3	-	66.8	-	9	0.10
$Y-MnO_x$	3.0	-	69.3	-	19	0.16
$CeMnO_x$	-	58.9	22.6	1.2	59	0.24
$Y/CeMnO_x$	2.8	56.8	21.8	1.2	50	0.21
$Y-CeMnO_x$	2.1	57.8	19.0	1.2	62	0.24

2.1. Textural Characteristics

Table 1 presents the values of specific surface area (SSA) and total pore volume of the samples determined from low-temperature nitrogen adsorption data. Manganese oxide-based samples are characterized by relatively low values of SSA (from 9 to 19 m^2/g) and total pore volume (from 0.10 to 0.16 cm^3/g), while the samples based on cerium oxide and mixed cerium and manganese oxides are characterized by rather high values of SSA (within 32–43 and 50–62 m^2/g, respectively) and total pore volume (within 0.14–0.16 and 0.21–0.24 cm^3/g, respectively). In general, a comparison of undoped and Y-doped samples indicates that the Y introduction using the one-pot citrate sol-gel method leads to an increase in both SSA and pore volume of the obtained materials, while the Y introduction via the impregnation of undoped oxides is accompanied by a significant decrease in the SSA with a slight change in the pore volume.

2.2. XRD Analysis

Figure 1 shows the XRD patterns for the samples, and Table 2 lists the phase composition of the samples and the characteristics of crystalline phases according to the XRD data.
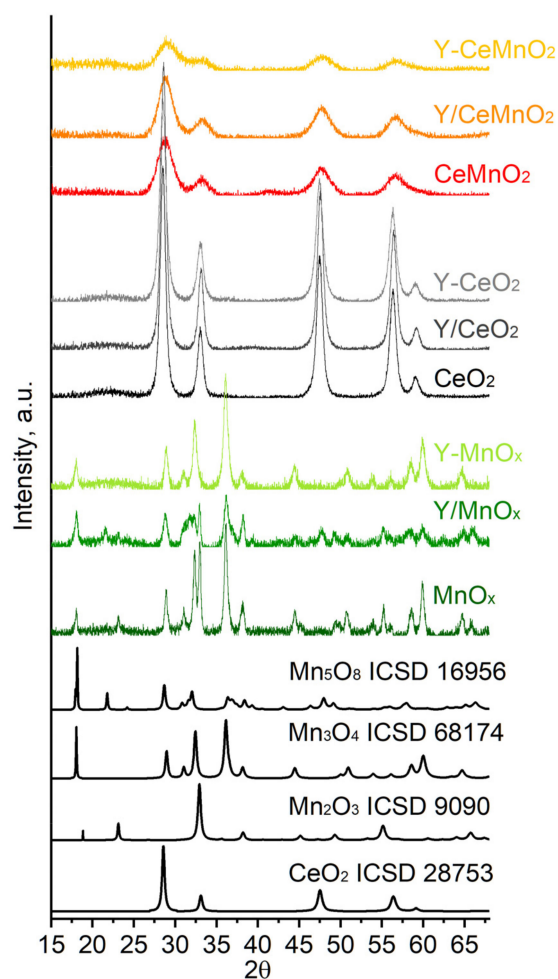
Figure 1. XRD patterns for samples.

Table 2. Phase composition of samples and structural parameters of crystalline phases.

| Sample | Phase Composition | | Structural Parameters | | | | | | D_{XRD}, nm |
	Phase	wt.%	S.G.	Symmetry	a, Å	b, Å	c, Å	β, °	
CeO_2	fluorite	100	Fm-3m	cubic	5.41	5.41	5.41	90	18
Y/CeO_2	fluorite	100	Fm-3m	cubic	5.40	5.40	5.40	90	18
$Y-CeO_2$	fluorite	100	Fm-3m	cubic	5.41	5.41	5.41	90	15
MnO_x	Mn_3O_4	75	I41/amd	tetragonal	5.76	5.76	9.46	90	33
	Mn_2O_3	25	Ia-3	cubic	9.41	9.41	9.41	90	61
Y/MnO_x	Mn_3O_4	34	I41/amd	tetragonal	5.76	5.76	9.47	90	48
	Mn_2O_3	11	Ia-3	cubic	9.42	9.42	9.42	90	64
	Mn_5O_8	55	C12/m1	monoclinic	10.42	5.73	4.87	109.9	24
$Y-MnO_x$	Mn_3O_4	100	I41/amd	tetragonal	5.76	5.76	9.45	90	28
$CeMnO_x$	fluorite	100	Fm-3m	cubic	5.38	5.38	5.38	90	5
$Y/CeMnO_x$	fluorite	100	Fm-3m	cubic	5.38	5.38	5.38	90	5
$Y-CeMnO_x$	fluorite	100	Fm-3m	cubic	5.38	5.38	5.38	90	4

For the unmodified MnO_x sample, the formation of primarily tetragonal Mn_3O_4 (75 wt.%) with some cubic Mn_2O_3 (25 wt.%) was observed. The tetragonal Mn_3O_4 with lattice parameters a = 5.76 Å and c = 9.46 Å was rather dispersed (mean crystallite size was ~33 nm), while the Mn_2O_3 phase with the lattice parameter a = 9.41 Å was coarse

(mean crystallite size was ~61 nm). In general, the amount of cubic Mn_2O_3 in the undoped sample depended on thermal treatment, with the increase in calcination temperature up to 650 °C resulting in the formation of only the Mn_2O_3 phase (Figure S1, in the Supplementary Materials). The MnO_x modification via impregnation resulted in the formation of monoclinic Mn_5O_8 as the main crystalline phase (55 wt.%) with crystal lattice parameters a = 10.42 Å, b = 5.73 Å, c = 4.87 Å, and β = 109.9° and a crystallite size of 24 nm in the Y/MnO_x sample. Along with the monoclinic phase, tetragonal Mn_3O_4 (34 wt.%) and some cubic Mn_2O_3 (11 wt.%) oxides were also formed. Finally, the MnO_x modification during sol-gel synthesis resulted in the formation of a single-phase Mn_3O_4 oxide, which was stable even after calcination at 650 °C (Figure S1, in the Supplementary Materials). The lattice parameters of the tetragonal Mn_3O_4 phase in the $Y-MnO_x$ sample were practically unchanged as compared with the unmodified MnO_x sample.

According to the XRD data, only a phase with a fluorite structure was revealed in the unmodified CeO_2, $CeMnO_x$, and Y-modified Y/CeO_2, $Y-CeO_2$, $Y/CeMnO_x$, and $Y-CeMnO_x$ samples. In the case of the CeO_2 sample, the fluorite phase was characterized by a lattice parameter a of 5.41 Å and an average crystallite size of 18 nm. In the case of the $CeMnO_x$ sample, the fluorite phase was characterized by a lower lattice parameter a = 5.40–5.38 Å and an average crystallite size of 5–7 nm as compared with the CeO_2 sample. The observed decrease in lattice parameter can be caused by the substitution of Ce^{4+}/Ce^{3+} ions with smaller Mn^{4+}/Mn^{3+} ions in the fluorite lattice [29,30]. Modification of both CeO_2 and $CeMnO_x$ samples with Y did not strongly affect the lattice parameter of the fluorite phase, which can be due to the low modifier content; however, the Y introduction during the sol-gel synthesis was accompanied by a decrease in the average crystallite size.

2.3. Raman Spectroscopy

The structural features of the samples were additionally studied by Raman spectroscopy. Figure 2 shows the Raman spectra for the samples.

Raman spectra for MnO_x and $Y-MnO_x$ samples are similar and contain weak bands at 262, 309, and 360 cm^{-1}, and an intense one at 644 cm^{-1}, which are characteristic of Mn_3O_4 with the spinel structure [31–34]. The intense band at 644 cm^{-1} is assigned to the A_{1g} mode, and the weak bands at 263, 308, and 360 cm^{-1} are referred to as the E_g, B_{2g}, and E_g modes, respectively [32]. In the case of the Y/MnO_x sample obtained by MnO_x impregnation, the spectrum contains the bands at 170, 222, 262, 390, 427, 475, 495, 531, 577, 623_{sh}, and 644 cm^{-1} characteristic of the Mn_5O_8 phase [35], which is consistent with the XRD data. The observed transition of Mn_3O_4 to Mn_5O_8 in the Y/MnO_x sample and Mn_3O_4 stability in the $Y-MnO_x$ sample are associated with different Y distributions, with the Y introduction through the sol-gel method resulting in the stabilization of the Mn_3O_4 phase.

The spectrum for the CeO_2 sample contains the bands at 263, 404_{sh}, 464, 590, and 827 cm^{-1} typical for a fluorite-type ceria [36,37]. The intense band at 464 cm^{-1} is the F_{2g} band associated with the Ce–O stretching in the $[CeO_8]$ cubic subcell, while the weak bands at 263, 404, and 590 cm^{-1} correspond to overtones, and the one at 827 cm^{-1} is due to the surface peroxide O_2^{2-} structures. The Y introduction in ceria during the sol-gel synthesis leads to the appearance of well-defined bands at 547 and 600 cm^{-1} in the spectrum for the $Y-CeO_2$ sample. These bands are associated with the Y^{3+} incorporation into CeO_2 [38–40]. The band at 600 cm^{-1} (band D_2) is associated with defect modes generated in ceria due to Ce^{4+} replacement by trivalent M^{3+} ions (M^{3+} = Ce^{3+}, Gd^{3+}, La^{3+}, Y^{3+}, etc.) and is assigned to defects with O_h symmetry [38–40]. The band at 547 cm^{-1} (band D_1) is associated with defects, including the oxygen vacancy, with a symmetry different from that of the O_h point group [39,40]. In the case of Y introduction in ceria via impregnation, the spectrum for the Y/CeO_2 sample does not contain the bands at 547 and 600 cm^{-1}, which indicates the predominant formation of undoped ceria as well as Y distribution primarily in the surface and subsurface layers.
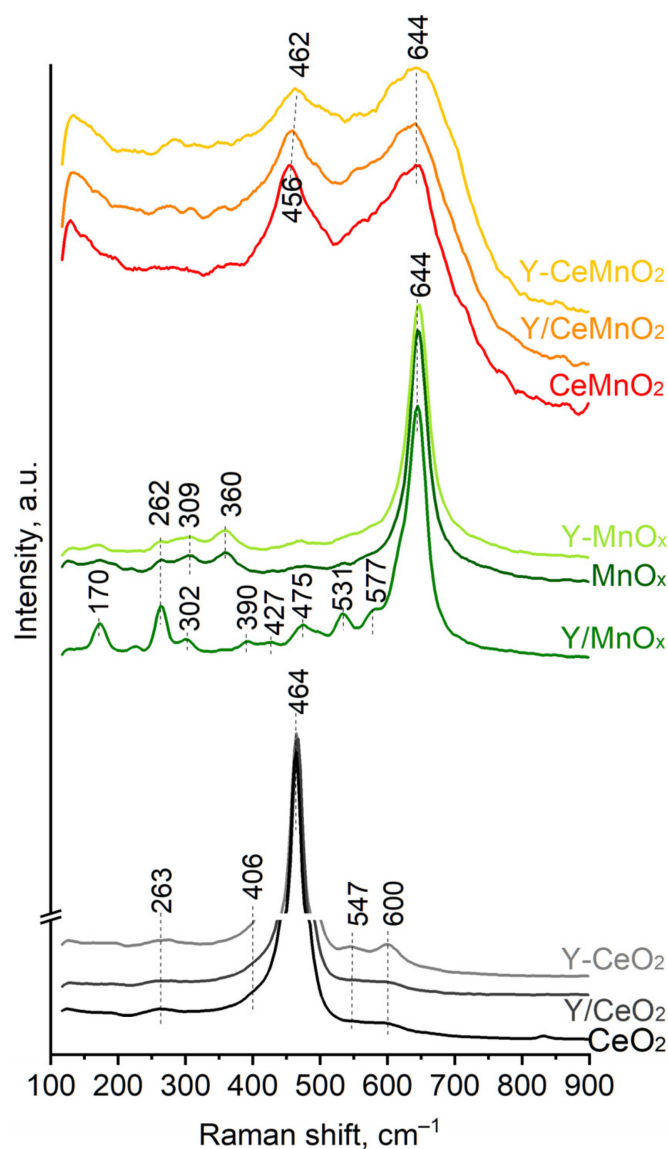
Figure 2. Raman spectra for samples.

The Raman spectra for $CeMnO_x$, $Y/CeMnO_x$, and $Y/CeMnO_x$ samples contain two intense broad bands with maxima at 456–462 and 644 cm^{-1} due to the stretching of Ce-O in ceria and Mn-O in manganese oxides, respectively. On the shoulders of these peaks as well as in the region below 400 cm^{-1}, weak bands due to overtones and defects in CeO_2 and other modes in Mn_3O_4, Mn_2O_3, and Mn_5O_8 are distinguishable. A strong broadening of the bands indicates a high dispersion of ceria and manganese oxides present in the samples, which is additionally confirmed by the HR TEM data showing the nanodomain structure for such samples (Figure 3). Therefore, the Raman spectra indicate the formation of a mixture of highly dispersed ceria and manganese oxide in the $CeMnO_x$, $Y/CeMnO_x$, and $Y/CeMnO_x$ samples but not a solid solution based on the fluorite phase as indicated by the XRD data. However, the partial incorporation of Mn as well as Y into the ceria fluorite phase cannot be excluded. This is consistent with our recent study on $Ag/CeMnO_x$ catalysts, where a "patchwork" domain microstructure composed of nanocrystallites enriched by either Mn or Ce was revealed for the mixed oxide support [28].
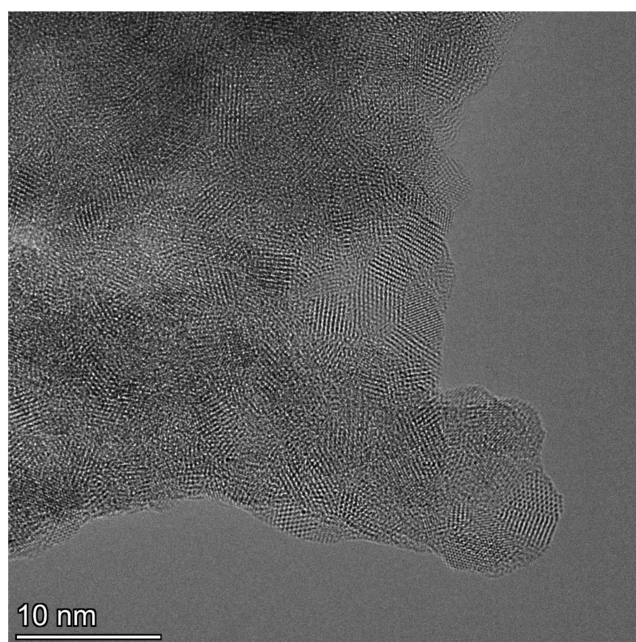
Figure 3. Typical HR TEM image for nanodomain structure of the CeMnO$_x$ sample.

2.4. H$_2$-TPR

Reducibility is one of the most important parameters influencing the SCR activity of the catalysts. For this reason, the reducibility of samples was investigated by H$_2$-TPR. Figure 4 represents the TPR profiles. As shown in the figure, two peaks at 491 and 868 °C appear in the H$_2$-TPR curve for CeO$_2$, which can be assigned to the surface/subsurface and bulk reduction of CeO$_2$, respectively [41]. Doping with yttrium leads to a shift of both reduction peaks to the low-temperature region independently of the method of ceria doping. Doping ceria with Y^{3+} (whose ionic radius is 1.02 Å) leads to the production of oxygen vacancies; in this way, the oxygen mobility and, consequently, the redox properties of ceria are changed [42]. Additionally, the profiles for Y-CeO$_2$ and Y/CeO$_2$ samples exhibit a well-defined shoulder at 313 °C that can be attributed to the reduction of Y-promoted ceria surface. A comparison of the TPR profiles shows that there are no substantial differences resulting from the method of yttrium introduction; this suggests that the distribution of yttrium in the bulk or in the surface and subsurface layers of the fluorite phase does not significantly influence the reduction process.

The TPR profile for the MnO$_x$ sample contains two low-intense peaks at 246 and 365 °C and an intense one at 518 °C. These results are consistent with the previously reported data and with the XRD and Raman spectroscopy data indicating Mn$_2$O$_3$ and Mn$_3$O$_4$ to be the primary active phases for NO reduction in MnO$_x$ catalysts. As reported in the literature, manganese oxide reduction can occur through a three-step process: MnO$_2$→Mn$_2$O$_3$→Mn$_3$O$_4$→MnO [43,44]. Specifically, the peaks observed at lower temperatures (<450 °C) correspond to the two-step reduction of MnO$_2$ (MnO$_2$ to Mn$_2$O$_3$ and Mn$_2$O$_3$ to Mn$_3$O$_4$, respectively); the peak at higher temperatures is attributed to the complete reduction of Mn$_3$O$_4$ to MnO [45]. Subsequent reduction of MnO to Mn^0 is generally not observed even up to reduction temperatures above 700 °C since this reduction is characterized by a higher negative reduction potential [46]. Thereby, the reduction peaks at 246 and 365 °C in the TPR profile for the MnO$_x$ sample are attributed to the reduction of coarse Mn$_2$O$_3$ particles to Mn$_3$O$_4$ on the surface and in the bulk, respectively, while the peak at 518 °C is assigned to Mn$_3$O$_4$ reduction to MnO.
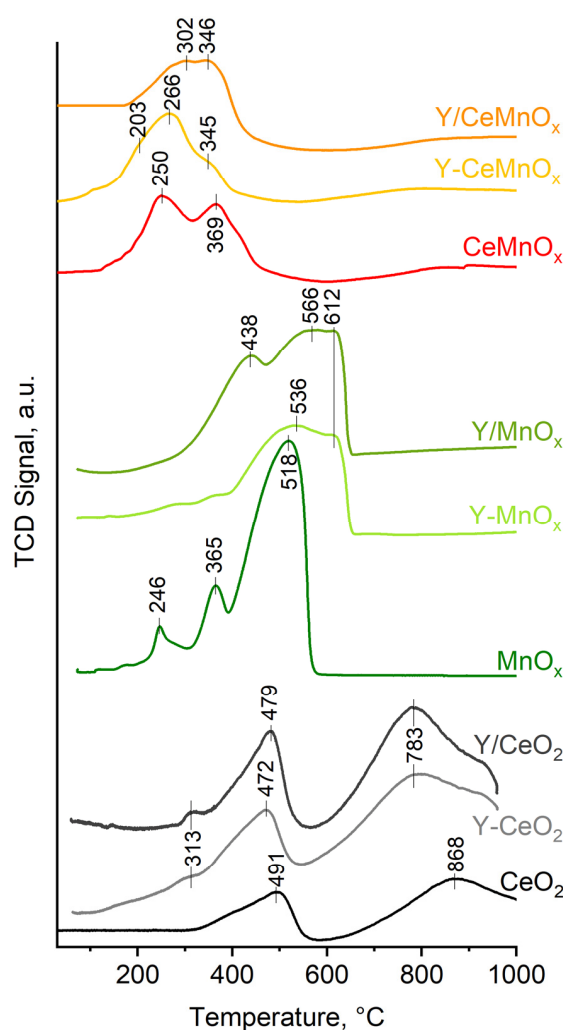
Figure 4. Temperature-programmed reduction profiles for samples.

The Y doping via one-pot sol-gel synthesis results in hydrogen consumption only at temperatures above 400 °C, with practically no reduction peaks being observed at lower temperatures. A wide peak at 536 °C with a shoulder at 612 °C is attributed to the reduction of the Y-doped Mn_3O_4 phase in accordance with the XRD data. In the case of Y doping via MnO_x impregnation, the TPR profile contains a new peak at 438 °C along with a high temperature peak at 566 °C with a shoulder at 612 °C. In accordance with the phase composition of the Y/MnO_x sample, this peak can be attributed to Mn_5O_8 reduction to Mn_3O_4.

Compared with the reducibility of undoped and Y-doped CeO_2 and MnO_x, the reduction temperatures of the mixed $CeMnO_x$ oxides are shifted towards lower temperatures. The decrease in the reduction temperature indicates that the reducibility of MnO_x and CeO_2 has been promoted, resulting in better mobility of the oxygen species, which improves the redox performance of the catalyst [47,48]. Based on the XRD results, introducing moderate amounts of Mn can generate more lattice defects and oxygen-free places, develop oxygen migration, transformation, and release capacities, and improve the redox capacity of the catalyst. The Y doping results in some changes within the same temperature interval in the TPR profiles for Y-$CeMnO_x$ and Y/$CeMnO_x$ samples, suggesting that some differences in the phase composition of the nanodomains of the oxide composites may occur. The yttrium introduction via the sol-gel method in general results in improving the reducibility of Y-$CeMnO_x$, while its introduction via the impregnation technique results in some hindered reducibility. This finding also seems to be caused by a different yttrium distribution, with impregnation techniques resulting in its distribution primarily on the surface.

2.5. Catalytic Performance

The obtained catalysts were studied in the NO SCR with NH_3 in the temperature range of 25 to 400 °C. Figure 5 shows the catalytic activity of the oxide catalysts. The NO conversion increases as the temperature rises, while the N_2 selectivity exhibits the opposite trend. SCR activity generally decreases in the following order: $CeMnO_x$ > $Y\text{-}CeMnO_x$ > $Y/CeMnO_x$ > MnO_x > $Y\text{-}MnO_x$ > Y/MnO_x > $Y\text{-}CeO_2$ > Y/CeO_2 > CeO_2. With the Y addition, the catalytic efficiency increases nonlinearly in various catalysts. Thus, CeO_2 shows a noticeable catalytic activity above 200 °C, but the NO conversion observed within 200–400 °C does not exceed 28%. The NO conversion at 200–400 °C increases for the Y-doped samples prepared by the one-pot sol-gel method.
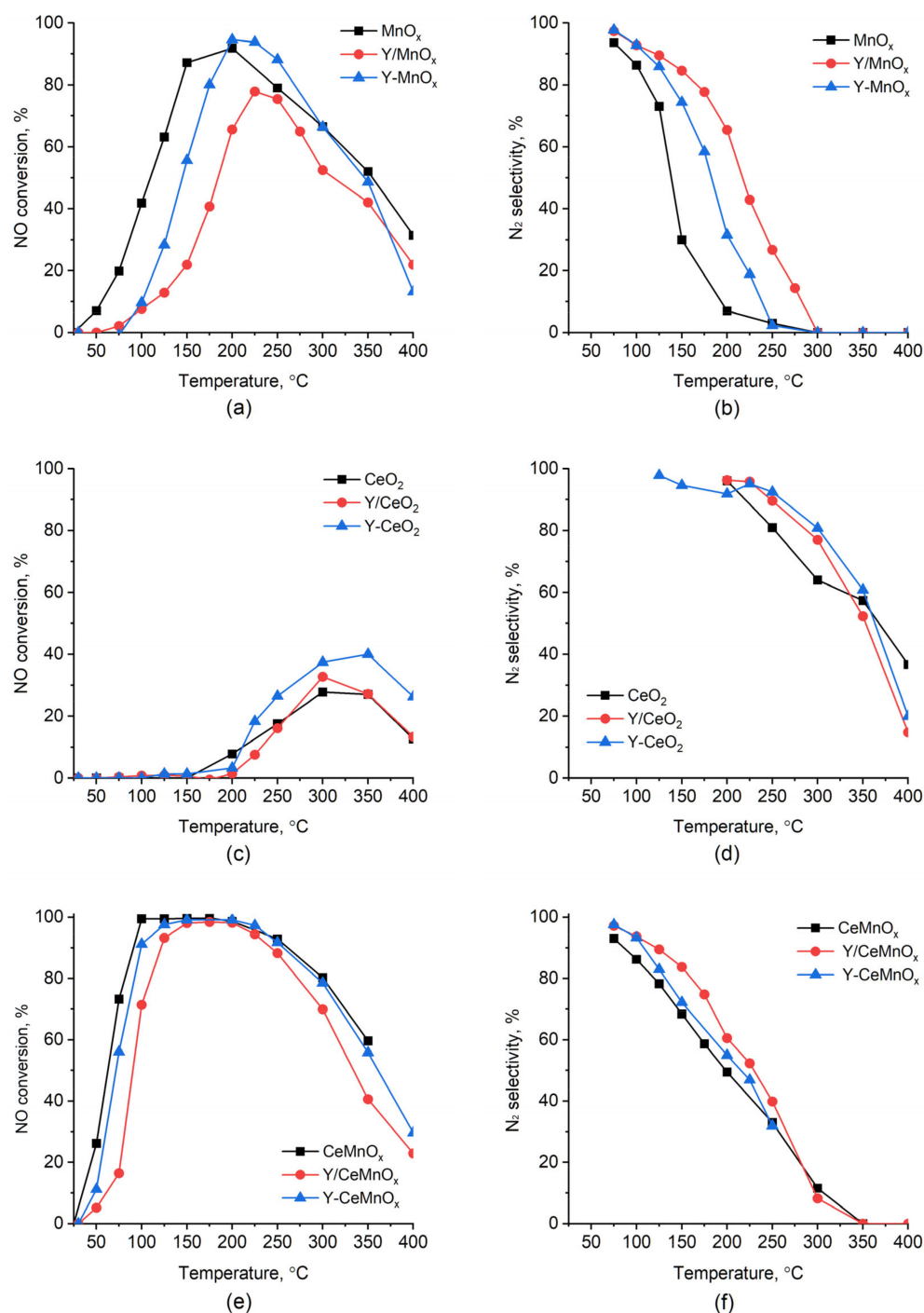

Figure 5. NO conversion (**a**,**c**,**e**) and N_2 selectivity (**b**,**d**,**f**) over undoped and Y-doped samples.

The MnO_x-based samples feature a higher NO conversion than those based on CeO_2. The MnO_x sample shows a noticeable catalytic activity already at 50 °C that goes through its maximum at 200 °C. However, the NO conversion over the MnO_x catalyst only reaches 91.8% at 200 °C. The Y doping results in a decrease in the catalytic activity of the Y-MnO_x sample below 200 °C, but the NO conversion is promoted to 94.6% at 200 °C. For the Y/MnO_x catalyst, the Y doping results in a remarkable decrease in the catalytic activity below 225 °C, with the highest NO conversion of 78% being observed at 225 °C. This is consistent with hindering the manganese oxide reducibility in the Y-doped samples, with the phase composition of the Y-doped samples also affecting their activity. In the Y/MnO_x sample, the monoclinic Mn_5O_8 phase consisting of Mn^{2+} and Mn^{4+} [35] seems to be less active as compared with the tetragonal Mn_3O_4 phase consisting of Mn^{2+} and Mn^{3+} [32] in the Y-MnO_x sample, which indicates the importance of the Mn^{3+} presence in the catalyst.

The catalytic activity is greatly improved for the $CeMnO_x$-based mixed oxide catalysts. In fact, a significant NO conversion (26%) is observed for the $CeMnO_x$ sample at 50 °C, and it reaches 100% at 100–200 °C. However, in both cases, the sample doping with Y does not enhance the catalytic activity of the mixed oxide catalysts. For the Y-$CeMnO_x$ sample, the effect of Y doping on the NO conversion is negligible. The NO conversion remains almost constant between 100 and 200 °C, which is accompanied by the narrowing of the activity window for the Y/$CeMnO_x$ sample. The latter can be caused by the formation of the less active monoclinic Mn_5O_8 phase in the Y/$CeMnO_x$ sample, as in the case of Y/MnO_x.

The so far reported differences in NO conversion between undoped oxides, Y-doped samples prepared by impregnation, and those synthesized using the one-pot sol-gel method can be attributed to several factors. It is likely that the one-pot method favors a more homogeneous Y distribution in the sample than the impregnation one. The Y-doped samples prepared by the one-pot method are characterized by higher SSA and lower crystal sizes than those prepared by impregnation, while the impregnation method results in the sample sintering. Both methods should generate a great number of structural defects in ceria due to the Y^{3+} introduction in the surface/subsurface layer or bulk of the fluorite phase, resulting in an improvement in the sample reducibility. However, the one-pot method results in stabilization of the tetragonal Mn_3O_4 ($Mn^{2+}Mn^{3+}_2O_3$) phase, while the impregnation method results in the formation of the monoclinic Mn_5O_8 ($Mn^{2+}_2Mn^{4+}_3O_8$) phase, accompanied by a hindering of the sample reducibility in the temperature range of ~100–400 °C.

An ideal NH_3-SCR catalyst should exhibit not only high conversion but also high selectivity towards N_2 to avoid the emission of harmful nitrogen oxides such as NO_2 and N_2O. Among all the investigated oxides, MnO_x and $CeMnO_x$ show higher NO_x conversion than CeO_2, but for all samples, the N_2 selectivity drops drastically with the temperature increase, as confirmed also by the N_2 yield of the samples (Figures 5 and 6). The Y doping improves the N_2 selectivity, which, in turn, results in enhanced catalyst efficiency at temperatures above ~125 °C. Such an effect is more evident for the Y-doped MnO_x oxides, which exhibit higher N_2 selectivity than the undoped sample. However, the maximum N_2 yield shifts to higher temperatures. Regarding the Y-doped $CeMnO_x$ samples, the one-pot-prepared Y-oxide gives almost the same N_2 selectivity curve, while a slightly enhanced selectivity and N_2 yield were registered between ~125 and 175 °C for the Y/$CeMnO_x$ sample (Figures 5 and 6). As for CeO_2 and Y-doped ceria oxides, the N_2 yield increases to a small extent for the Y-CeO_2 sample in the range of 200–400 °C.

To sum up, the Y addition to CeO_2, MnO_x, and $CeMnO_x$ influences the N_2 selectivity and yield in a different manner depending on the preparation method used and the nature of the manganese oxide formed. The higher selectivity of the Y-doped MnO_x and $CeMnO_x$ samples is consistent with the lower sample reducibility.

The observed decrease in N_2 selectivity and N_2 yield registered for the CeO_2, MnO_x, and $CeMnO_x$ oxides and the corresponding Y-doped samples can be attributed to the competitive oxidation of ammonia (NH_3-SCO) catalyzed by manganese [49] and cerium oxides, which leads to the formation of NO, NO_2, and N_2O and consequently decreases

the selectivity. To confirm this hypothesis, Figure 7 presents the temperature dependencies of NH_3, NO, NO_2, and N_2O concentrations for the most efficient $CeMnO_x$, Y-$CeMnO_x$, and $Y/CeMnO_x$ samples. The NH_3 concentration rapidly decreased by increasing the temperature and was totally consumed at ~200 °C, resulting in an increase in the N_2O concentration between ~150 and 300 °C, according to Refs. [50,51]. Then, above 250 °C, the presence of NO and NO_2 was also observed.
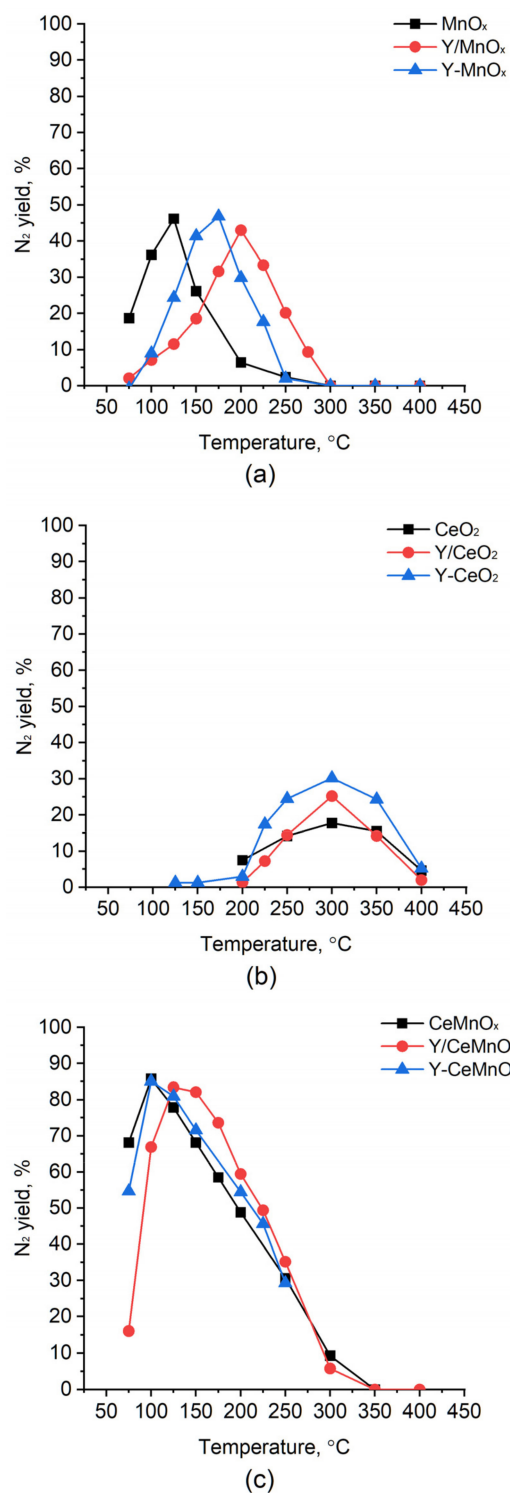
(a)

(b)

(c)

Figure 6. N_2 yields over undoped and Y-doped samples based on MnO_x (**a**), CeO_2 (**b**) and $CeMnO_x$ (**c**).
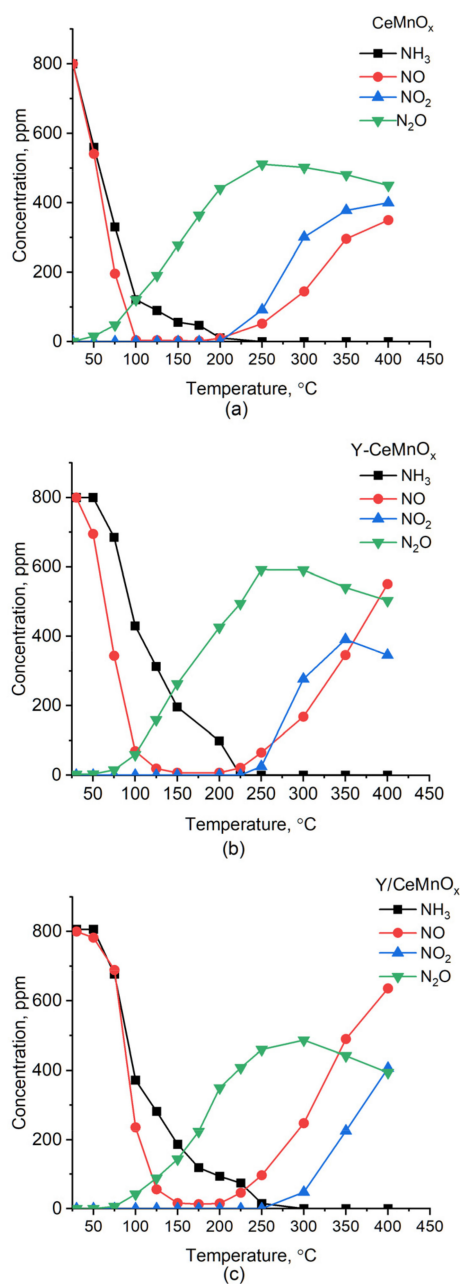
Figure 7. Comparison of NH_3, NO, NO_2, and N_2O concentrations for $CeMnO_x$ (**a**), $Y\text{-}CeMnO_x$ (**b**), and $Y/CeMnO_x$ (**c**) samples.

2.6. Role of Redox Properties and Surface Acidity

According to the literature [23,50–53], the low-temperature NH_3-SCR of NO can proceed over the oxide catalysts through the Eley–Rideal or Langmuir–Hinshelwood mechanisms. Both mechanisms include NH_3 adsorption on Lewis acid sites followed by its transformation to active species (NH_2, NH, etc.) and/or interaction with the adsorbed NO or the one from the gas phase to form N_2. The NO adsorption can be accompanied by its transformation into an active NO_2 species. The oxidative transformation of both adsorbed NH_3 and NO molecules was shown to occur via the interaction with the lattice oxygen [50,51] and with gaseous oxygen taking part in the catalyst reoxidation. However, an abundance of the labile lattice oxygen species on the catalyst surface led to the N_2O overoxidation [50]. Thereby, both the redox properties and surface acidity of the oxide catalysts play a crucial role in the NH_3-SCR of NO.

NH$_3$-TPD was used to study the surface acidity of the MnO$_x$- and CeMnO$_x$-based samples as more efficient ones. Figure 8 shows the NH$_3$-TPD profiles for the samples, while in Table 3 the maximal NH$_3$ desorption temperatures and the amounts of desorbed NH$_3$ (µmol g^{-1}) are listed for each sample. All supports exhibit a large NH$_3$ desorption peak with a maximum in the range of 200–300 °C. According to the literature, the low-temperature peaks can be assigned to the desorption of ammonia chemisorbed on the weak Lewis acidic sites [54,55]. The amount of NH$_3$ desorbed from the CeMnO$_x$ support (243.0 µmol g^{-1}) is higher than that for MnO$_x$ (52.0 µmol g^{-1}), indicating that this sample has a higher acidic capacity and, thus, is able to activate NH$_3$ in the range of temperature typical for ammonia SCR in accordance with the catalytic results. For the Y-doped samples, the total acidity and strength of the acid sites increase notably as compared with MnO$_x$ and CeMnO$_x$ samples, with the samples prepared by the one-pot method being more acidic than those obtained by impregnation. The enhanced acidity can be attributed to the presence of Y^{3+} cations on the surface, which act as weak Lewis acid sites and can affect the surface acidity of the samples [56].
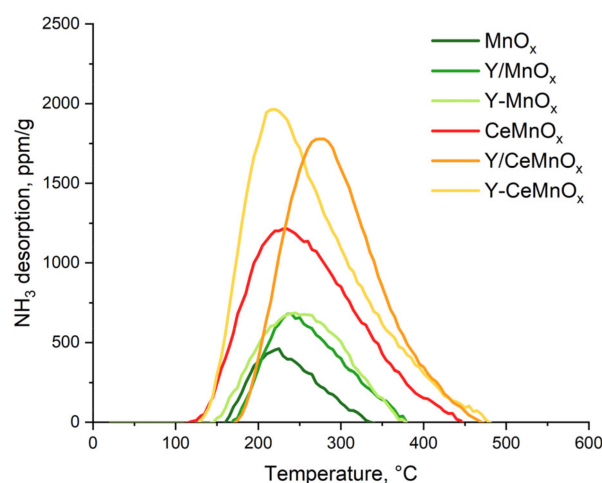

Figure 8. The NH$_3$-TPD profiles for samples.

Table 3. Results of NH$_3$-TPD for samples.

Sample	T (°C)	NH$_3$ Desorbed (µmol g^{-1})
MnO$_x$	225	52
Y-MnO$_x$	245	105
Y/MnO$_x$	240	89
CeMnO$_x$	235	243
Y-CeMnO$_x$	225	370
Y/CeMnO$_x$	280	318

Despite the high surface acidity as compared with the undoped samples, the observed decrease of the catalytic activity for Y-MnO$_x$, Y/MnO$_x$, and Y/CeMnO$_x$ samples was attributed to their hindered reducibility. This resulted in the hindering of the oxidation of adsorbed NH$_3$ with labile lattice oxygen species to active species (NH$_2$, NH, etc.) at low temperatures and prevented its overoxidation to more NO at high temperatures. Thereby, to improve the catalytic performance of the oxide catalyst towards the NH$_3$-SCR of NO, optimization of their redox properties and surface acidity is required. In this respect, the CeMnO$_x$ composite materials are good candidates for developing an effective catalyst for SCR of NO, with their doping being a promising way for further catalyst enhancement.

3. Materials and Methods

3.1. Sample Preparation

Unmodified and Y-modified (2 wt.%) oxide samples were prepared. The unmodified oxide supports were prepared by a citrate method, while two approaches were used to modify oxide supports with Y, including one-pot citrate method (series 1) and incipient wetness impregnation of undoped oxides with water solution of $Y(NO_3)_3$ (series 2).

3.1.1. Sample Preparation Using Sol-Gel Citrate Method

The unmodified and Y-modified (series 1) CeO_2, MnO_x and CeO_2–MnO_x supports with a molar ratio of Ce/Mn = 1 were synthesized by the citrate method. Analytical-grade $Ce(NO_3)_3·6H_2O$, $Mn(NO_3)_2·6H_2O$, and $Y(NO_3)_3·6H_2O$ salts were used as Ce, Mn, and Y precursors, and citric acid ($C_6H_8O_7·H_2O$) was used as a complexing agent. All reagents were used directly without any further purification. The concentrated aqueous solutions of $Ce(NO_3)_3$ (0.84 mol/L), $Mn(NO_3)_2$ (2.6 mol/L), and $Y(NO_3)_3$ (1.84 mol/L) were prepared from metal nitrates for further use.

The individual or mixed solution of the corresponding metal nitrates was added to an aqueous solution of citric acid with vigorous stirring, followed by heating to 55–60 °C and constant stirring to form sol. The citric acid-to-metal (Ce, Mn, Y) molar ratio was 1.2 (pH of solution was ~1–2). The obtained sol was held at 60 °C with constant stirring for 2 h to form a gel, followed by the gel's aging in a drying furnace overnight at 80 °C for undoped samples or for 10–18 h at 60 °C for the Y-doped samples.

Then the resulting gel was heated (10 deg/min) up to 120 °C and additionally dried at 120 °C for 5 h in a muffle furnace, followed by heating (5 deg/min) up to 500 °C and calcination of the dried gel in air at 500 °C for 3 h.

The samples synthesized by this approach were designated as CeO_2, MnO_x, $CeMnO_x$, Y-CeO_2, Y-MnO_x, and Y-$CeMnO_x$.

3.1.2. Sample Modification Using Impregnation Technique

The Y-modified oxide supports (series 2) were additionally prepared by incipient wetness impregnation of undoped oxide supports Ce-3, Mn-2, CeMn-2 with the $Y(NO_3)_3$ aqueous solutions. The required volume of the $Y(NO_3)_3$ solution was added to the powder of oxide support, followed by a thorough mixing of the paste formed. The impregnated sample was dried at room temperature for 5 h and then at 80 °C for 6 h in a drying furnace. Then it was heated (10 deg/min) up to 500 °C and calcined at 500 °C for 2 h in the muffle furnace.

The samples synthesized by this approach were designated as Y/CeO_2, Y/MnO_x, and $Y/CeMnO_x$.

3.2. Characterization

The prepared samples were studied by several characterization methods, including nitrogen adsorption/desorption at −196 °C, X-ray analysis (XRD), Raman spectroscopy, hydrogen temperature-programmed reduction (TPR), and NH_3-TPD.

3.2.1. Low-Temperature Nitrogen Adsorption/Desorption

The specific surface area, total pore volume, and average pore diameter were determined from the low-temperature nitrogen adsorption/desorption (at −196 °C) using the TriStar II 3020 specific analyzer (Micromeritics, Norcross, GA, USA). Prior to experiments, all samples were degassed at 200 °C in a vacuum (10^{-2} Torr) for 2 h using the laboratory degassing station VacPrep Degasser (Micromeritics, Norcross, GA, USA). The specific surface area was determined by the Brunauer-Emmett-Teller (BET) method, and the pore volume and pore size distributions were determined by the Barrett-Joyner-Halenda (BJH) method using the desorption branch of the adsorption-desorption isotherm.

3.2.2. XRD

The XRD patterns for the samples were recorded by the X-ray diffractometer XRD-7000 (Shimadzu, Kyoto, Japan) with monochromatic CuKα radiation (1.54 Å) in the angle range of 10–70° 2θ and a scanning rate of 0.02°/s. The data were obtained using Bragg–Brentano geometry. Crystalline Si (a = 5.4309 Å, λ = 1.540562 Å) was used as an external standard for diffractometer calibration. The phase composition was analyzed using the PDF-4 database (Release 2021 RDB). To refine the lattice parameters and determine the crystalline size, the POWDER CELL 2.4 full profile analysis program was used.

3.2.3. Raman Spectroscopy

Raman spectra were obtained on the InVia spectrometer (Renishaw, Wotton-under-Edge, UK) equipped with the DM 2500M microscope (Leica, Wetzlar, Germany) with a 50× objective. For excitation, lasers with wavelengths of 532 nm and a power of 100 mW were used; the spectral resolution was 2 cm^{-1}. To prevent changes in the samples, only 5% of the full laser power and 50% beam defocus were applied.

3.2.4. Transmission Electron Microscopy

Transmission electron microscopy (TEM) data were obtained using the double aberration-corrected electron microscope Themis Z (Thermo Fisher Scientific, Eindhoven, The Netherlands) operated at 200 kV. The samples for the TEM study were dispersed ultrasonically and deposited on copper grids covered with a holey carbon film.

3.2.5. H_2-TPR

Hydrogen temperature-programmed reduction (TPR) measurements were carried out with the Automated Catalyst Characterization System AutoChem 2950HP (Micromeritics, Norcross, GA, USA) equipped with a thermal conductivity detector (TCD). About 0.1 g of a sample was used for each measurement. The samples were pre-treated with a mixture of 5 vol% O_2 in He at 50 mL/min, heated up (10 °C/min) to 400 °C, and held at this temperature for 30 min. After cooling down to room temperature, the gas mixture of 5 vol.% H_2 in Ar was introduced at 30 mL/min into the sample tube and was also used as a reference gas. During the analysis, the temperature was increased up to 1000 °C at a rate of 10 °C/min. The effluent gas was analyzed with a TCD.

3.2.6. NH_3-TPD

Temperature-programmed desorption of ammonia (NH_3-TPD) was performed using the Micromeritics Autochem 2910 equipped with an ultraviolet gas analyzer (ABB, Limas 11, ABB S.p.a. Milano, Italy). Prior to the ammonia adsorption experiment, the sample was pretreated in a He flow at 200 °C for 30 min. After cooling down to room temperature, a stream of 5% NH_3/He (30 mL/min) was flowed over the sample for 1 h. To remove the physically adsorbed ammonia, the sample was purged in flowing He (100 mL/min) at 100 °C for 1 h. Then, after cooling down to room temperature, ammonia desorption was monitored with the UV gas analyzer. After flowing He (30 mL/min) and heating up to 600 °C (rate of 10 °C/min), holding time at 600 °C was 30 min. A cold trap was used before the gas detection system to condense any water desorbed from the sample. The ammonia concentration in terms of ppm NH_3 desorbed/g_{cat} under He flow (30 mL/min) was plotted versus time and temperature.

3.3. Activity Tests in SCR of NO by NH_3

The NH_3-SCR tests were performed in a fixed-bed, continuous-flow U quartz reactor with an inner diameter of 12 mm. The feed gas, consisting of 800 ppm NO + 800 ppm NH_3 + 10 vol% O_2 in He, was flowed over the catalyst (120 mg) at a rate of 50 mL·min^{-1}, equivalent to a weight hourly space velocity (WHSV) of 25,000 mL g^{-1} h^{-1}. The conversion values were measured as a function of temperature from 25 °C to 500 °C with a heating rate of 5 °C/min, holding for 40 min at each temperature that was increased by steps of

50 °C. The inlet and outlet gas compositions were analyzed by the ABB detectors: infrared (Limas 11) for NO, N_2O, NO_2, NH_3, paramagnetic (Magnos 206) for O_2. Each test was repeated three times to estimate its reproducibility. The error obtained was less than 2% for the reported values.

The NO conversion, N_2 selectivity, and N_2 yield were calculated according to the following equations [57]:

$$\text{NO conversion (\%)} : \frac{[NO]_{in} - [NO]_{out}}{[NO]_{in}} \times 100;$$

$$N_2 \text{ selectivity (\%)} : \left(1 - \frac{[NO_2]out + 2[N_2O]out}{[NO]in + [NH_3]in - [NH_3]out - [NO]out}\right) \times 100 ;$$

$$N_2 \text{ yield (\%)} : \frac{\text{NO conversion} \times N_2 \text{ selectivity}}{100}.$$

4. Conclusions

The CeO_2, MnO_x, $CeMnO_x$, and yttrium-doped supports were successfully synthesized through a combination of the citrate sol-gel method for support synthesis and incipient wetness impregnation with $Y(NO_3)_3$ aqueous solution for the Y deposition, or via a one-pot sol-gel synthesis approach. Activity tests confirmed that the $CeMnO_x$ support exhibited superior low-temperature performance compared with MnO_x or CeO_2 oxides. Specifically, full NO conversion was achieved between 75 and 200 °C, with the selectivity to N_2 being close to 90% at low temperatures; however, above 150 °C, the selectivity rapidly decreased due to the ammonia oxidation. The results suggested that the $CeMnO_x$ mixed oxide may have considerable potential for the development of NH_3-SCR technologies for the reduction of NO emissions, although further improvements in N_2 selectivity are needed. While Y doping did not enhance the NO conversion activity of the mixed oxide, it widened the selectivity range for MnO_x oxides. The remarkable NO SCR activity of the $CeMnO_x$ sample in such a large temperature window can be attributed to its excellent reduction capability between ~200 and 350 °C, likely resulting from highly active oxygen species derived from dispersed nanocrystallites enriched by either Mn or Ce oxides in intimate contact, thus enhancing the low-temperature catalytic properties.

Both Y-doped CeO_2 and MnO_x samples, prepared by the one-pot method, achieved slightly higher NO conversion values than the corresponding undoped oxides, although the curve was shifted to higher temperatures in the case of Y-MnO_x. Conversely, no improvement of the low-temperature performance for Y/CeO_2 by incipient wetness impregnation or even a negative effect was registered for the Y/MnO_x sample.

Further studies are required to gain a complete understanding of the reaction mechanism governing the enhanced NO SCR performance of the $CeMnO_x$ mixed oxide, optimize the catalyst composition in terms of the Ce:Mn molar ratio, and further improve the physical-chemical properties. Nevertheless, our study provides promising results for the future development of effective and eco-friendly catalysts for NO emission control.

References

1. Gómez-García, M.A.; Pitchon, V.; Kiennemann, A. Pollution by Nitrogen Oxides: An Approach to NO_x Abatement by Using Sorbing Catalytic Materials. *Environ. Int.* **2005**, *31*, 445–467. [CrossRef]

2. Reşitoĝlu, I.A.; Altinişik, K.; Keskin, A. The Pollutant Emissions from Diesel-Engine Vehicles and Exhaust Aftertreatment Systems. *Clean Technol. Environ. Policy* **2015**, *17*, 15–27. [CrossRef]

3. Flagiello, D.; Esposito, M.; Di Natale, F.; Salo, K. A Novel Approach to Reduce the Environmental Footprint of Maritime Shipping. *J. Mar. Sci. Appl.* **2021**, *20*, 229–247. [CrossRef]

4. Chmielewski, A.G.; Sun, Y.; Zimek, Z.; Bułka, S.; Licki, J. Mechanism of NO_x removal by electron beam process in the presence of scavengers. *Radiat. Phys. Chem.* **2002**, *65*, 397–403. [CrossRef]

5. Wang, S.; Xu, S.; Gao, S.; Xiao, P.; Jiang, M.; Zhao, H.; Huang, B.; Liu, L.; Niu, H.; Wang, J.; et al. Simultaneous removal of SO_2 and NO_x from flue gas by low-temperature adsorption over activated carbon. *Sci. Rep.* **2021**, *11*, 11003. [CrossRef] [PubMed]

6. Flagiello, D.; Di Natale, F.; Erto, A.; Lancia, A. Oxidative Scrubber for NO_X Emission Control Using $NaClO_2$ Aqueous Solutions. *Chem. Eng. Trans.* **2021**, *86*, 397–402. [CrossRef]

7. Han, L.; Cai, S.; Gao, M.; Hasegawa, J.Y.; Wang, P.; Zhang, J.; Shi, L.; Zhang, D. Selective Catalytic Reduction of NO_x with NH_3 by Using Novel Catalysts: State of the Art and Future Prospects. *Chem. Rev.* **2019**, *119*, 10916–10976. [CrossRef]

8. Alemany, L.J.; Berti, F.; Busca, G.; Ramis, G.; Robba, D.; Toledo, G.P.; Trombetta, M. Characterization and Composition of Commercial V_2O_5-WO_3-TiO_2 SCR Catalysts. *Appl. Catal. B Environ.* **1996**, *10*, 299–311. [CrossRef]

9. Wu, H.; He, M.; Liu, W.; Jiang, L.; Cao, J.; Yang, C.; Yang, J.; Peng, J.; Liu, Y.; Liu, Q. Application of Manganese-Containing Soil as Novel Catalyst for Low-Temperature NH_3-SCR of NO. *J. Environ. Chem. Eng.* **2021**, *9*, 105426. [CrossRef]

10. Li, Y.; Zhang, Z.; Zhao, X.; Liu, Z.; Zhang, T.; Niu, X.; Zhu, Y. Effects of Nb-Modified $CeVO_4$ to Form Surface Ce-O-Nb Bonds on Improving Low-Temperature NH_3-SCR DeNOx Activity and Resistance to SO_2 & H_2O. *Fuel* **2023**, *331*, 125799. [CrossRef]

11. Chen, L.; Liu, J.; Hu, W.; Gao, J.; Yang, J. Vanadium in Soil-Plant System: Source, Fate, Toxicity, and Bioremediation. *J. Hazard. Mater.* **2021**, *405*, 124200. [CrossRef] [PubMed]

12. Ding, L.; Wang, Y.; Qian, L.; Qi, P.; Xie, M.; Long, H. Flue Gas DeNOxing Spent V_2O_5-WO_3/TiO_2 Catalyst: A Review of Deactivation Mechanisms and Current Disposal Status. *Fuel* **2023**, *338*, 127268. [CrossRef]

13. Casapu, M.; Kröcher, O.; Elsener, M. Screening of Doped MnO_x-CeO_2 Catalysts for Low-Temperature NO-SCR. *Appl. Catal. B Environ.* **2009**, *88*, 413–419. [CrossRef]

14. Shi, J.W.; Gao, C.; Liu, C.; Fan, Z.; Gao, G.; Niu, C. Porous MnOx for Low-Temperature NH_3-SCR of NO_x: The Intrinsic Relationship between Surface Physicochemical Property and Catalytic Activity. *J. Nanoparticle Res.* **2017**, *19*, 194. [CrossRef]

15. Kapteijn, F.; Singoredjo, L.; Andreini, A.; Moulijn, J.A. Activity and Selectivity of Pure Manganese Oxides in the Selective Catalytic Reduction of Nitric Oxide with Ammonia. *Appl. Catal. B Environ.* **1994**, *3*, 173–189. [CrossRef]

16. Kašpar, J.; Fornasiero, P.; Graziani, M. Use of CeO_2-Based Oxides in the Three-Way Catalysis. *Catal. Today* **1999**, *50*, 285–298. [CrossRef]

17. Sun, H.; Park, S.J. Recent Advances in MnO_x/CeO_2-Based Ternary Composites for Selective Catalytic Reduction of NO_x by NH_3: A Review. *Catalysts* **2021**, *11*, 1519. [CrossRef]

18. Wu, X.; Yu, H.; Weng, D.; Liu, S.; Fan, J. Synergistic Effect between MnO and CeO_2 in the Physical Mixture: Electronic Interaction and NO Oxidation Activity. *J. Rare Earths* **2013**, *31*, 1141–1147. [CrossRef]

19. Wang, C.; Yu, F.; Zhu, M.; Tang, C.; Zhang, K.; Zhao, D.; Dong, L.; Dai, B. Highly Selective Catalytic Reduction of NO_x by MnO_x–CeO_2–Al_2O_3 Catalysts Prepared by Self-Propagating High-Temperature Synthesis. *J. Environ. Sci.* **2019**, *75*, 124–135. [CrossRef]

20. Qi, G.; Yang, R.T.; Chang, R. MnOx-CeO_2 Mixed Oxides Prepared by Co-Precipitation for Selective Catalytic Reduction of NO with NH_3 at Low Temperatures. *Appl. Catal. B Environ.* **2004**, *51*, 93–106. [CrossRef]

21. Xu, L.; Li, X.S.; Crocker, M.; Zhang, Z.S.; Zhu, A.M.; Shi, C. A Study of the Mechanism of Low-Temperature SCR of NO with NH_3 on MnO_x/CeO_2. *J. Mol. Catal. A Chem.* **2013**, *378*, 82–90. [CrossRef]

22. Chen, L.; Ren, S.; Xing, X.; Yang, J.; Li, J.; Yang, J.; Liu, Q. Effect of MnO_2 crystal types on CeO_2@MnO_2 oxides catalysts for low-temperature NH_3-SCR. *J. Environ. Chem. Eng.* **2022**, *10*, 108239. [CrossRef]

23. Chen, Z.; Ren, S.; Zhou, Y.; Li, X.; Wang, M.; Chen, L. Comparison of Mn doped CeO_2 with different exposed facets for NH_3-SCR at low temperature. *J. Energy Inst.* **2022**, *105*, 114–120. [CrossRef]

24. Wu, Z.; Jin, R.; Liu, Y.; Wang, H. Ceria Modified $MnOx/TiO_2$ as a Superior Catalyst for NO Reduction with NH_3 at Low-Temperature. *Catal. Commun.* **2008**, *9*, 2217–2220. [CrossRef]

25. Zhou, B.; Xi, K.; Fan, L.J.; Zhou, Y.; Wang, Y.; Zhu, Q.L.; Lu, H.F. A Comparative Study on Ce–Pr and Ce–Mn Mixed Oxide Catalysts toward Soot Catalytic Combustion. *Appl. Catal. A Gen.* **2018**, *562*, 1–10. [CrossRef]

26. Jiang, Z.; Chen, C.; Ma, M.; Guo, Z.; Yu, Y.; He, C. Rare-Earth Element Doping-Promoted Toluene Low-Temperature Combustion over Mesostructured CuMCeO: X (M = Y, Eu, Ho, and Sm) Catalysts: The Indispensable Role of in Situ Generated Oxygen Vacancies. *Catal. Sci. Technol.* **2018**, *8*, 5933–5942. [CrossRef]

27. Zhang, S.; Liu, X.; Zhong, Q.; Yao, Y. Effect of y Doping on Oxygen Vacancies of TiO_2 Supported MnO_X for Selective Catalytic Reduction of NO with NH_3 at Low Temperature. *Catal. Commun.* **2012**, *25*, 7–11. [CrossRef]

28. La Greca, E.; Kharlamova, T.S.; Grabchenko, M.V.; Consentino, L.; Savenko, D.Y.; Pantaleo, G.; Kibis, L.S.; Stonkus, O.A.; Vodyankina, O.V.; Liotta, L.F. Ag Catalysts Supported on CeO_2, MnO_2 and $CeMnO_x$ Mixed Oxides for Selective Catalytic Reduction of NO by C_3H_6. *Nanomaterials* **2023**, *13*, 873. [CrossRef] [PubMed]

29. Huang, H.; Liu, J.; Sun, P.; Ye, S.; Liu, B. Effects of Mn-Doped Ceria Oxygen-Storage Material on Oxidation Activity of Diesel Soot. *RSC Adv.* **2017**, *7*, 7406–7412. [CrossRef]

30. Murugan, B.; Ramaswamy, A.V.; Srinivas, D.; Gopinath, C.S.; Ramaswamy, V. Nature of Manganese Species in $Ce_{1-x}Mn_xO_{2-\delta}$ Solid Solutions Synthesized by the Solution Combustion Route. *Chem. Mater.* **2005**, *17*, 3983–3993. [CrossRef]

31. Yang, X.; Wang, X.; Zhang, G.; Zheng, J.; Wang, T.; Liu, X.; Shu, C.; Jiang, L.; Wang, C. Enhanced Electrocatalytic Performance for Methanol Oxidation of Pt Nanoparticles on Mn_3O_4-Modified Multi-Walled Carbon Nanotubes. *Int. J. Hydrogen Energy* **2012**, *37*, 11167–11175. [CrossRef]

32. Larbi, T.; Doll, K.; Manoubi, T. Density Functional Theory Study of Ferromagnetically and Ferrimagnetically Ordered Spinel Oxide Mn_3O_4. A Quantum Mechanical Simulation of Their IR and Raman Spectra. *J. Alloys Compd.* **2016**, *688*, 692–698. [CrossRef]

33. Gao, T.; Fjellvåg, H.; Norby, P. A Comparison Study on Raman Scattering Properties of α- and β-MnO_2. *Anal. Chim. Acta* **2009**, *648*, 235–239. [CrossRef] [PubMed]

34. Julien, C.M.; Massot, M.; Poinsignon, C. Lattice Vibrations of Manganese Oxides: Part I. Periodic Structures. *Spectrochim. Acta Part A Mol. Biomol. Spectrosc.* **2004**, *60*, 689–700. [CrossRef] [PubMed]

35. Gao, T.; Norby, P.; Krumeich, F.; Okamoto, H.; Nesper, R.; Fjellvåg, H. Synthesis and Properties of Layered-Structured Mn_5O_8 Nanorods. *J. Phys. Chem. C* **2010**, *114*, 922–928. [CrossRef]

36. Schilling, C.; Hofmann, A.; Hess, C.; Ganduglia-Pirovano, M.V. Raman Spectra of Polycrystalline CeO_2: A Density Functional Theory Study. *J. Phys. Chem. C* **2017**, *121*, 20834–20849. [CrossRef]

37. Schilling, C.; Ganduglia-Pirovano, M.V.; Hess, C. Experimental and Theoretical Study on the Nature of Adsorbed Oxygen Species on Shaped Ceria Nanoparticles. *J. Phys. Chem. Lett.* **2018**, *9*, 6593–6598. [CrossRef]

38. Taniguchi, T.; Watanabe, T.; Sugiyama, N.; Subramani, A.K.; Wagata, H.; Matsushita, N.; Yoshimura, M. Identifying Defects in Ceria-Based Nanocrystals by UV Resonance Raman Spectroscopy. *J. Phys. Chem. C* **2009**, *113*, 19789–19793. [CrossRef]

39. Nakajima, A.; Yoshihara, A.; Ishigame, M. Defect-Induced Raman Spectra in Doped CeO_2. *Phys. Rev. B* **1994**, *50*, 13297–13307. [CrossRef]

40. Derevyannikova, E.A.; Kardash, T.Y.; Kibis, L.S.; Slavinskaya, E.M.; Svetlichnyi, V.A.; Stonkus, O.A.; Ivanova, A.S.; Boronin, A.I. The Structure and Catalytic Properties of Rh-Doped CeO_2 Catalysts. *Phys. Chem. Chem. Phys.* **2017**, *19*, 31883–31897. [CrossRef]

41. Grabchenko, M.V.; Mamontov, G.V.; Zaikovskii, V.I.; La Parola, V.; Liotta, L.F.; Vodyankina, O.V. Design of Ag-CeO_2/SiO_2 Catalyst for Oxidative Dehydrogenation of Ethanol: Control of Ag–CeO_2 Interfacial Interaction. *Catal. Today* **2019**, *333*, 2–9. [CrossRef]

42. Ilieva, L.; Venezia, A.M.; Petrova, P.; Pantaleo, G.; Liotta, L.F.; Zanella, R.; Kaszkur, Z.; Tabakova, T. Effect of Y Modified Ceria Support in Mono and Bimetallic Pd-Au Catalysts for Complete Benzene Oxidation. *Catalysts* **2018**, *8*, 283. [CrossRef]

43. Trawczyński, J.; Bielak, B.; Miśta, W. Oxidation of Ethanol over Supported Manganese Catalysts—Effect of the Carrier. *Appl. Catal. B Environ.* **2005**, *55*, 277–285. [CrossRef]

44. Stobbe, E.R.; De Boer, B.A.; Geus, J.W. The Reduction and Oxidation Behaviour of Manganese Oxides. *Catal. Today* **1999**, *47*, 161–167. [CrossRef]

45. Zhan, S.; Zhu, D.; Qiu, M.; Li, Y. Highly efficient Removal of NO with Ordered Mesoporous Manganese Oxide at Low Temperature. *RSC Adv.* **2015**, *5*, 29353–29361. [CrossRef]

46. Ye, Q.; Zhao, J.; Huo, F.; Wang, J.; Cheng, S.; Kang, T.; Dai, H. Nanosized Ag/α-MnO_2 Catalysts Highly Active for the Low-Temperature Oxidation of Carbon Monoxide and Benzene. *Catal. Today* **2011**, *175*, 603–609. [CrossRef]

47. Tang, X.; Chen, J.; Li, Y.; Li, Y.; Xu, Y.; Shen, W. Complete Oxidation of Formaldehyde over Ag/MnOx–CeO2 Catalysts. *Chem. Eng. J.* **2006**, *118*, 119–125. [CrossRef]

48. Wang, K.; Liu, X.; Tu, S.; Zhang, L.; Li, W.; Jiang, C.; Ye, D. Low Temperature Catalytic Performance of Manganese and Cerium Complex Oxide Catalyst towards Toluene. *IOP Conf. Ser. Mater. Sci. Eng.* **2020**, *729*, 012069. [CrossRef]

49. Consentino, L.; Pantaleo, G.; Parola, V.L.; Migliore, C.; Greca, E.L.; Liotta, L.F. NH3-NO SCR Catalysts for Engine Exhaust Gases Abatement: Replacement of Toxic V_2O_5 with MnO_x to Improve the Environmental Sustainability. *Top. Catal.* **2022**, 1–10. [CrossRef]

50. Gao, F.; Liu, Y.; Sani, Z.; Tang, X.; Yi, H.; Zhao, S.; Yu, Q.; Zhou, Y. Advances in Selective Catalytic Oxidation of Ammonia (NH_3-SCO) to Dinitrogen in Excess Oxygen: A Review on Typical Catalysts, Catalytic Performances and Reaction Mechanisms. *J. Environ. Chem. Eng.* **2021**, *9*, 104575. [CrossRef]

51. Yang, S.; Liao, Y.; Xiong, S.; Qi, F.; Dang, H.; Xiao, X.; Li, J. N_2 Selectivity of NO Reduction by NH_3 over MnO_x-CeO_2: Mechanism and Key Factors. *J. Phys. Chem. C* **2014**, *118*, 21500–21508. [CrossRef]

52. Liao, Y.; Liu, Z.; Li, Z.; Gao, G.; Ji, L.; Xu, H.; Huang, W.; Qu, Z.; Yan, N. The Unique CO Activation Effects for Boosting NH_3 Selective Catalytic Oxidation over $CuOx$–CeO_2. *Environ. Sci. Technol.* **2022**, *56*, 10402–10411. [CrossRef]

53. Jiang, Y.; Han, D.; Yang, L.; Yang, Z.; Ge, H.; Lin, R.; Wang, X. Improving the K resistance effectively of CeO_2-TiO_2 catalyst by Nb doping for NH_3-SCR reaction. *Process Saf. Environ. Prot.* **2022**, *160*, 876–886. [CrossRef]

54. Lee, S.M.; Park, K.H.; Hong, S.C. MnO_x/CeO_2-TiO_2 Mixed Oxide Catalysts for the Selective Catalytic Reduction of NO with NH3 at Low Temperature. *Chem. Eng. J.* **2012**, *195–196*, 323–331. [CrossRef]

55. Kharlamova, T.S.; Timofeev, K.L.; Salaev, M.A.; Svetlichnyi, V.A.; Vodyankina, O.V. Monolayer $MgVO_x$/Al_2O_3 catalysts for propane oxidative dehydrogenation: Insights into a role of structural, redox, and acid-base properties in catalytic performance. *Appl. Catal. A* **2020**, *598*, 117574. [CrossRef]

56. Zhang, Y.; Zhou, Y.; Shi, J.; Zhou, S.; Zhang, Z.; Zhang, S.; Guo, M. Propane Dehydrogenation over $PtSnNa$/La-Doped Al_2O_3 Catalyst: Effect of La Content. *Fuel Process. Technol.* **2013**, *111*, 94–104. [CrossRef]

57. Inomata, Y.; Mino, M.; Hata, S.; Kiyonaga, E.; Morita, K.; Hikino, K.; Yoshida, K.; Haruta, M.; Murayama, T. Low-temperature NH_3-SCR Activity of Nanoparticulate Gold Supported on a Metal Oxide. *J. Japan Pet. Inst.* **2019**, *62*, 234–243. [CrossRef]